Noise-free computational ghost imaging with pink noise speckle patterns

Xiaoyu Nie,[1,2,*] Fan Yang,[1,2,*] Xiangpei Liu,[1,3] Xingchen Zhao,[1] Reed Nessler,[1]
Zheng Li,[4] Tao Peng,[1,†] M. Suhail Zubairy,[1] and Marlan O. Scully[1,5,6]

[1]*Department of Physics and Astronomy, Texas A&M University, College Station, Texas, 77843, USA*
[2]*Physics Department, Xi'an Jiaotong University, Xi'an, Shaanxi 710049, China*
[3]*Hefei National Laboratory for Physics Science at the the Microscale and Department of Modern Physics, University of Science and Technology of China, Hefei, Anhui 230026, China*
[4]*State key Laboratory for Mesoscopic Physics, School of Physics, Peking University, Beijing 100871, China*
[5]*Baylor Research and Innovatuon Collaborative, Baylor University, Waco, 76706, USA*
[6]*Princeton University, Princeton, New Jersey 08544, USA*

(Dated: October 1, 2020)

Computational ghost imaging reconstructs an object by second order correlation measurement with the use of a single pixel detector. It normally requires a large number of speckle patterns to make an ensemble average to retrieve the desired images. In this work, we propose a pink noise speckle pattern illumination in the computational ghost imaging system. We then experimentally demonstrate high signal-to-noise ratio reconstructed images in the presence of a variety of noises. The results are also compared with the use of standard white noise. We show that under extreme noisy environment or pattern distortion, our method gives good quality image while traditional method fails.

I. INTRODUCTION

Ghost imaging (GI)[1–3], which can be realized in both quantum light and classical light, is an alternative to the system applying conventional digital cameras. By making the second-order correlation between the intensities of two light path, GI can significantly eliminate the interference from the media during the process of light propagation. One major ameliorated system, Computational Ghost Imaging (CGI), only employs one single element detector to reconstruct images[4, 5]. CGI also grants advantages in an expanding range of non-conventional applications such as wide spectrum imaging [6, 7] and depth mapping [8, 9]. Moreover, it can be applied to image with spatially variant and re-configurable resolution [10–12]. Yet notwithstanding those proliferating applications, compared to the traditional imaging by digital cameras, the rather low signal-to-noise ratio (SNR) and requirement of a large number of patterns in CGI are always unavoidable, which significantly restricted this method from spreading to more widespread area of applications.

In CGI systems, to reconstruct a fully sampled image, the minimum number of speckle patterns required is proportional to the independent pixel size of the object. At the same time, the lower the system frame-rate, the higher the SNR of the calculated image is [13, 14]. There are many schemes such as differential detection [15, 16], balanced detection [17], and micro-scanning techniques [13, 18, 19] being employed with CGI to decrease the influence of system noise, and further enhance SNR. On the other hand, the orthogonal sampling strategies [20, 21], compressive sensing ghost imaging [22–24], and deep learning ghost imaging[25] have been recently explored to obtain a better shaped image in general based on the result from CGI. These methods help shorten the signal acquisition time through reducing the total number of correlation measurements, especially some experiments performed with fast spatial light modulators (SLM), such as the digital micro-mirror devices (DMD) [7], LED arrays [26, 27] or optical phased array [28]. However, applying these technologies means we should know information from the imaging system in advance. For example, the compressive sensing ghost imaging needs prior understanding of the scene such as sparsity constraints to guide the image reconstruction; the deep learning ghost imaging method requires us preparing thousands of training figures to develop the convolutional neural networks; the hybrid few-pixel computational ghost imaging systems, in which the frame-rate is increased by a factor of 4 [29], also have to exploited the accessibility of loading image information onto both the spatial and temporal dimensions by operating a quadrant photo-detector. In a word, achieving high SNR results without knowing images information before sampling should be a meaningful goal worth to chase.

---

*These two authors contributed equally
†Electronic address: taopeng@tamu.edu

Pink noise describes the electronic noises[30], statistical structure of natural images[31], and it is also one of the most common signals in biological systems[32]. In this letter, we adapt the concept of pink noise in the spatial frequency domain of speckle patterns. We present an robustness CGI scheme with the pink noise speckle patterns. The measurements are performed under several environmental interference situations. We also compare the results of pink noise with white noise which has been commonly used in the last decade[33].

II. CHARACTERISTICS OF PINK NOISE SPECKLES

For ghost imaging, speckle patterns are generally scattered laser light from a ground glass diffuser[34], or use a spatial light modulator (SLM) to modulate the laser beam. Both are white noise speckles that obey Rayleigh statistics. Here we introduce the pink noise speckle patterns, in which the power of the spectrum decreases with spatial frequency. The power distribution of the spectrum is defined as $S(\omega) \propto \omega^n$, where n determines the color of the noise speckle generated. When $n = 0$, the output are white noise patterns; when $n = -1$, we have pink noise speckle patterns. A random phase is then assigned to each frequency component. At last, an inverse Fourier transformation is performed upon the spectrum to obtain pink and white noise gray-scale patterns. The results are shown in Fig. 1(a).

To simplify the calculation without loss of generality, we consider here the one-dimensional case, and the spatial intensity distribution of the speckles can be express as

$$I(x) = \sum_{0}^{\omega_0} S(\omega_i) \cos(\omega_i x + \phi_i). \tag{1}$$

Here, $S(\omega_i)$ is the power spectral density corresponding to the spatial frequency ω_i, ω_0 is the cut-off frequency used in the pattern production. ϕ_i is a random phase associated with ω_i and it varies uniformly in the range of $[0, 2\pi]$.

For white noise, we have $S(\omega) \propto C$, the first order correlation of white noise is then

$$G^{(1)}(x_1, x_2) = \langle E(x_1)E^*(x_2)\rangle = \int_0^{\omega_0} C\cos(\omega\tilde{x})d\omega \propto \omega_0 \operatorname{sinc}\omega_0\tilde{x}, \tag{2}$$

where $\tilde{x} \equiv x_2 - x_1$, and $I(x_1) \equiv G^{(1)}(x_1, x_1)$. The second order correlation is given by

$$\begin{aligned} G_w^{(2)}(x_1, x_2) &= \langle I(x_1)I(x_2)\rangle_w \\ &= \int_0^{\omega_0} C^2\cos(\omega\tilde{x})d\omega + |G_w^{(1)}(x_1, x_1)||G_w^{(1)}(x_2, x_2)| \\ &\propto \omega_0^2(1 + \operatorname{sinc}^2\omega_0\tilde{x}), \end{aligned} \tag{3}$$

The normalized intensity fluctuation correlation is defined as

$$\Gamma^{(2)}(x_1, x_2) \equiv \frac{\langle I(x_1)I(x_2)\rangle - \langle I(x_1)\rangle\langle I(x_2)\rangle}{\langle I(x_1)\rangle\langle I(x_2)\rangle}. \tag{4}$$

For white noise, we have

$$\Gamma_w^{(2)}(x_1, x_2) = \operatorname{sinc}^2(\omega_0\tilde{x}). \tag{5}$$

On the other hand, pink noise has the following properties[35]

$$G^{(1)}(x_1, x_2) = \int_{\omega_1}^{\omega_2} (C'/\omega)\cos(\omega\tilde{x})d\omega \propto C_i(\omega_2\tilde{x}) - C_i(\omega_1\tilde{x}), \tag{6}$$

where ω_1 is the lowest frequency allowed which follows the pink noise PDF, ω_2 is the upper bound frequency, and $C_i(x)$ is the cosine integral. The intensity correlation is given by

$$\begin{aligned} G_p^{(2)}(x_1, x_2) &= \langle I(x_1)I(x_2)\rangle_p \\ &= \int_{\omega_1}^{\omega_2} (C'/\omega)^2\cos(\omega\tilde{x})d\omega + |G_p^{(1)}(x_1, x_1)||G_p^{(1)}(x_2, x_2)|, \end{aligned} \tag{7}$$

From Eq. (4) we have:

$$\Gamma_p^{(2)}(x_1, x_2) \propto \frac{\cos\omega_1\tilde{x}}{\omega_1} - \frac{\cos\omega_2\tilde{x}}{\omega_2} + \tilde{x}[S_i(\omega_1\tilde{x}) - S_i(\omega_2\tilde{x})], \tag{8}$$

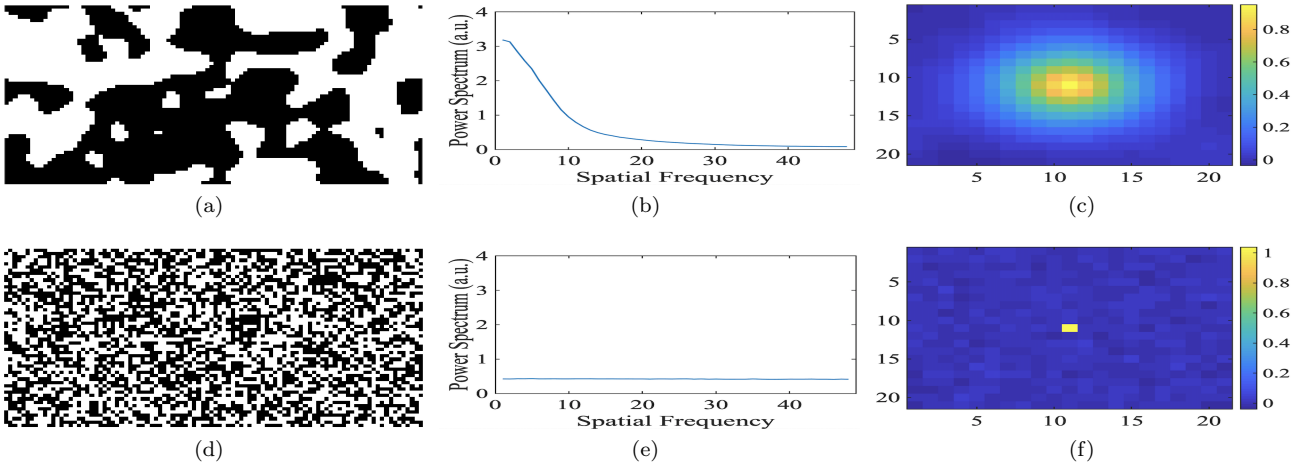

FIG. 1: (a),(b) and (c): two-dimensional noise pattern, power spectrum, and correlation map of customized pink pattern; (d),(e) and (f): two-dimensional noise pattern, power spectrum, and correlation map of standard white noise pattern. There exist cross-correlation between a pink noise pixel and its neighborhoods.

where $S_i(x)$ is the sine integral. This correlation function shows a much longer tail than white noise correlation as $\tilde{x}$ increases.

An application of the spectral intensity distribution corresponding to spatial frequency leads to a remarkable positive cross-correlation between pixels adjacent to each other. This is in contrast to white noise patterns where there is no relation between pixels and the cross-correlation is 0. To visualize this unique nature of pink noise, we randomly pick one pixel each from pink and white noise patterns, and calculate its cross-correlation and self-correlation. The striking difference can be seen form Fig. 1(c) for pink noise and Fig. 1(f) for white noise.

In the imaging system, we have the intensity from the bucket detector

$$\langle I_b \rangle \propto \langle \int dx_o E(x_o) E^*(x_o) |T(x_o)|^2 | \rangle, \tag{9}$$

and the intensity distribution on the object plane is

$$\langle I(x_o) \rangle = G^{(1)}(x_o, x_o) = \langle E(x_o) E^*(x_o) \rangle, \tag{10}$$

The second order imaging is determined by the correlation function

$$\langle \Delta I_b \Delta I(x_o) \rangle_w \propto \langle \int dx_o \Gamma_w^{(2)} |T(x_o)|^2 \rangle \propto |T(x_o)|^2. \tag{11}$$

The cross correlation of the light on the image plane diffracted from different pixels has zero contribution according to Eq. (11).

The second order correlation in the image measured with pink noise speckle pattern is :

$$\langle \Delta I_b \Delta I(x_o) \rangle_p \propto \langle \int dx_o \Gamma_p^{(2)}(x_0, x_0') |T(x_o)|^2 \rangle. \tag{12}$$

From Eq. (12) we notice that the situation is different due to the existence of cross correlation between light from different speckles as shown in Eq. (8). Intuitively, we see that all the image pixels which are next to each other, will contribute to cross-correlation with each pixel. This is in addition to the contribution of the auto correlations from each pixel. The overall second order signal strength is much increased, and the noise is largely suppressed due to the lack of correlation between other noises or the signals.

III. RESULTS

The experimental setup is shown in Fig. 2. A CW laser is used to illuminate the DMD where the noise patterns are loaded. The pattern generated by the DMD is then imaged onto the object plane. A CCD right after the object

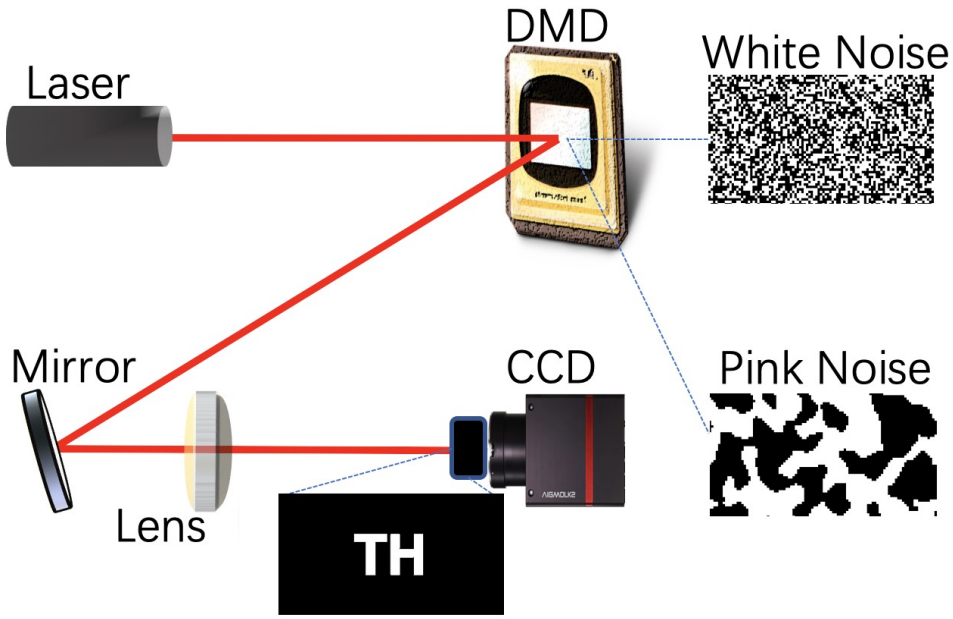

FIG. 2: Schematic of the basic setup for a CGI experiment without interference. A CW laser is reflected by the DMD where the noise patterns are loaded. The reflected laser with noise patterns propagates to the imaging surface by a lens. The object 'TH' is put close to the CCD, which is used as a bucket detector in all the experiments in this work.

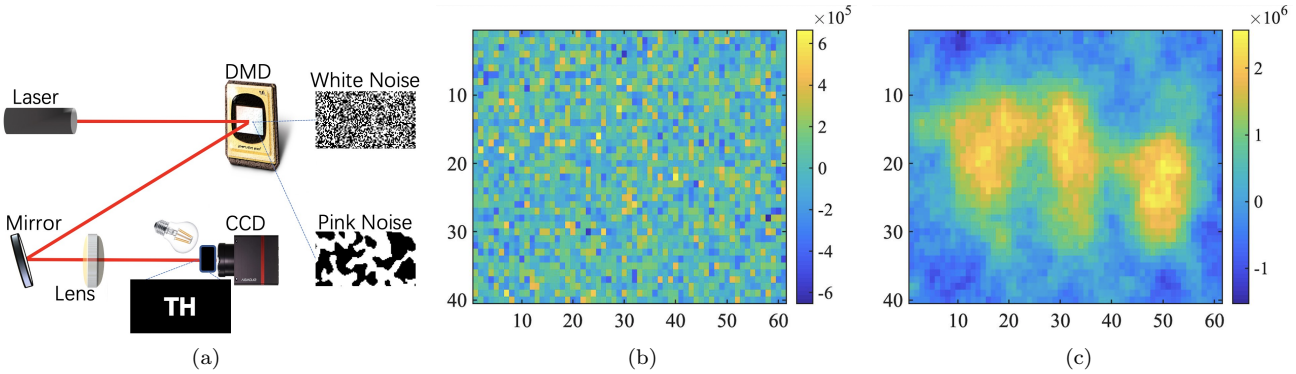

FIG. 3: (a). Schematic of the setup with environment noise introduced by a light bulb put in front of the object ; (b). CGI with white noise speckle illumination, 800 patterns are used for the ensemble average; (c) CGI with pink noise speckle illumination, 800 patterns are used for the ensemble average. The CGI with white noise is totally blurred due to the strong background noise, while the CGI with pink noise show clear retrieved image.

is used as a bucket detector, *i.e.*, only the total intensity on the CCD is used for the correlation measurement. The size of the noise pattern is 216 by 392 pixels, in which the independent changeable mirrors count for 4 by 4 pixels. In our experiment, the DMD contains tiny pixel-mirrors each measuring 16 μm $\times$ 16 μm. The noise pattern consists of 54 $\times$ 98 independent pixels (each pixel counts 4 $\times$ 4 DMD pixels). The object 'TH' contains a total of about 600 independent pixels.

A. Noise between source and object

The image quality of CGI depends largely on the total intensity array collected by the detector (the CCD in the present case). We therefore expect low noise level from both its own electronic noise and the environmental noise. However, both noises exist in the real applications. Here we use an incandescent lamp placed between DMD and the object to introduce disturbance to the noise pattern illumination on the object. The schematic of setup is shown in Fig. 3, We use 800 white and pink noise speckle patterns in the measurements. The results are shown in Fig. 3(b)

and Fig. 3(c), respectively. In order to compare those two methods quantitatively, we introduce the SNR defined as following

$$SNR = \frac{\mu_{sig}}{\sigma_{sig}}, \tag{13}$$

where the μ_{sig} is the average signal value and the σ_{sig} is the standard deviation of the signal. For the result of the pink noise CGI shown in Fig. 3(c), the SNR is ~ 4.40. The SNR of white noise CGI shown in Fig. 3(b) is ~ 0.87. So when there is strong environmental noise along the optical path, in between the light source and the object, it is not easy to retrieve the image through standard CGI scheme[27]. It is nevertheless shown here that the pink noise speckles can largely suppress the influence of such disturbance.

B. Noise and Diffuser between source and object

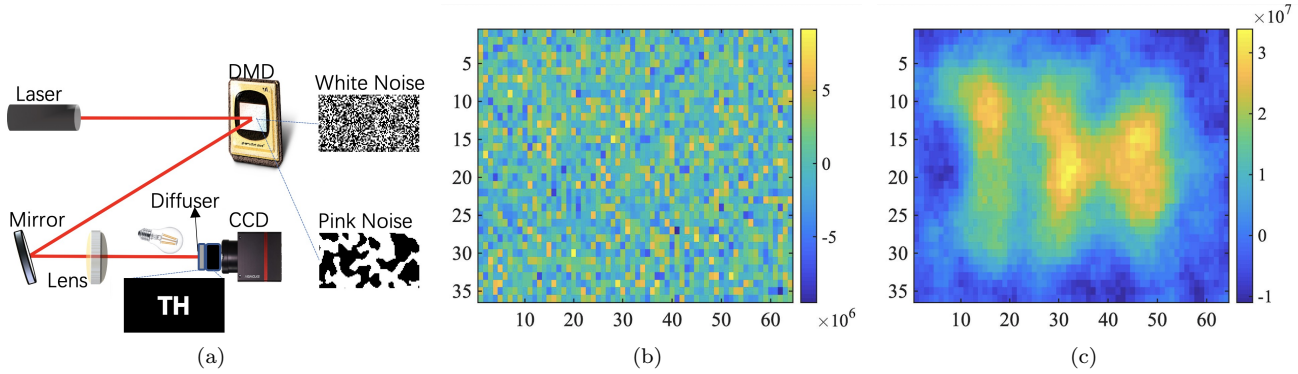

FIG. 4: (a). Schematic of the setup, a ground glass diffuser is put in front of the object to diffuse the speckle patterns, a light bulb is also put in front of the object to further introduce environment noise; (b). CGI with white noise speckle illumination, 800 patterns are used for the ensemble average; (c) CGI with pink noise speckle illumination, 800 patterns are used for the ensemble average. The CGI with white noise is totally blurred due to the strong background noise, while the CGI with pink noise show clear retrieved image.

In additional to the incandescent lamp, we add a ground glass diffuser between the lens and object to introduce diffraction and the background noise at the same time. This mimics the situation that the patterns are both smeared and buried in the background noise. The schematic is shown in Fig. 4. The CGI result of averaging 800 speckle patterns is shown in Fig. 4(b) for white noise and Fig. 4(c) for pink noise. The SNR of the white noise imaging is only 0.12, and it decreases a lot as compared to Sec. III A ($\text{SNR} \sim 0.87$). The SNR for pink noise is 4.13, which is comparable to the previous result ($\text{SNR} \sim 4.40$). So an introduction of the glass diffuser in the optical path decreases the image quality of white noise to a great extend, but it does not affect the pink noise much. This again is a demonstration of the robustness of pink noise CGI.

C. Noise between object and detector

To further explore adapted situations for pink noise CGI, we enhance the interference level by placing the incandescent lamp which produces strong white light noise between the object and the CCD. The setup presented in Fig. 5(a) is similar to Fig. 3(a), except for the location of the incandescent lamp. Here the noise distributes uniformly on the CCD plane to mimic a strong noise from the bucket detector. To be more specific, the noise intensity of each pixel is around 130 to 140 units, where the transmitted signal is only around 2 to 3 units.

The results are presented in Fig. 5(b) for white noise illumination and Fig. 5(c) for pink noise illumination. Here due to the extremely strong background noise at the detector, 10000 patterns are used to retrieve the image for both cases. This shows that the pink noise in CGI can reconstruct the image of the object, with $\text{SNR} \sim 3.97$. However the white noise speckle patterns fail to reconstruct the image at all, and the SNR is only 0.19.

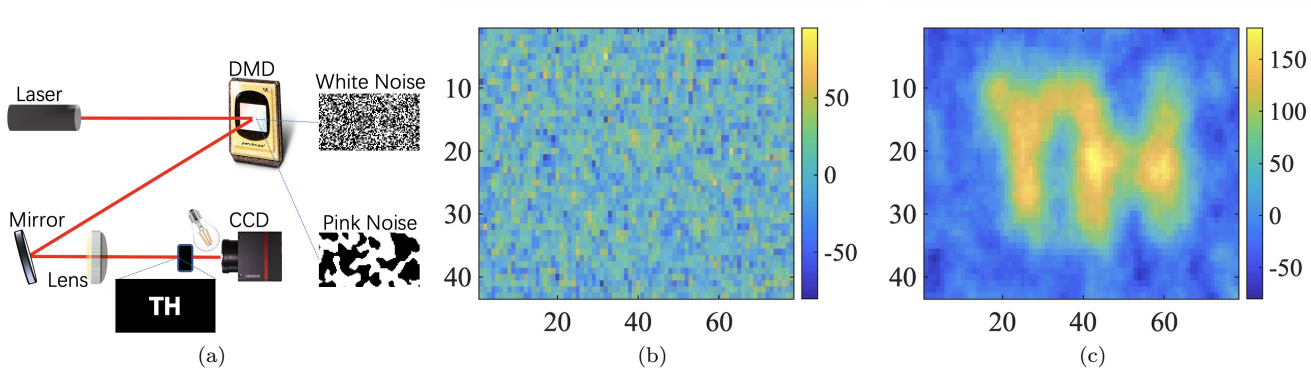

FIG. 5: (a). Schematic of the setup with environment noise introduced by a light bulb put in front of the detector; (b). CGI with white noise speckle illumination, 10000 patterns are used for the ensemble average; (c) CGI with pink noise speckle illumination, 10000 patterns are used for the ensemble average. The CGI with white noise is totally blurred due to the strong background noise, while the CGI with pink noise show clear retrieved image.

D. Diffraction of speckle patterns

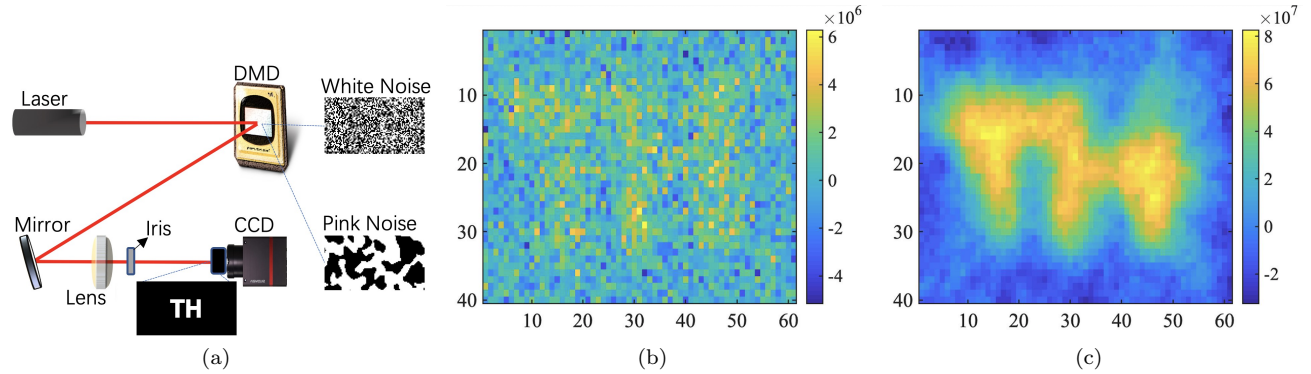

FIG. 6: (a). Schematic of the setup with an iris insert right after the lens. The diameter of the iris is 1000 μm. The speckle patterns are diffracted due to the iris; (b). CGI with white noise speckle illumination, 800 patterns are used for the ensemble average; (c) CGI with pink noise speckle illumination, 800 patterns are used for the ensemble average. The CGI with white noise is totally blurred due to the strong background noise, while the CGI with pink noise show clear retrieved image.

In this experiment, we put an iris right after the lens, which is used to image the speckle patterns on the object plane, as shown in Fig. 6(a). In the presence of the iris, the speckles can no longer maintain their spatial distribution as loaded on the DMD. Therefore the bucket detector recorded intensity is a mixture of desired speckles and unwanted speckles. The one-to-one correspondence of the CGI is no longer valid as shown in Fig. 6(b), the SNR from white noise speckle patterns is with an average of 800 patterns. The pink noise CGI, on the other hand, is still able to retrieve image of the object, as shown in Fig. 6(c). Here 800 patterns are used as well.

The results are presented in Fig. 5(b) for white noise illumination and Fig. 5(c) for pink noise illumination. This shows that the pink noise in CGI can clearly reconstruct the image of the object, and the SNR is 3.75. Due to the strong interference, the commonly used white noise pattern and no clear image, and the SNR is 0.88.

IV. CONCLUSION

In conclusion, we have developed a novel method to create pink noise speckle patterns, and apply it to the CGI system. Experimentally, the resulted SNR of pink noise CGI is always much better than the SNR of white noise CGI in the presence of different noise and obstacles interference. This work is of great significance for the practical application of CGI, due to its robustness.

Acknowledgments

This work was supported by Air Force Office of Scientific Research (Award No. FA9550-20-1-0366 DEF), Office of Naval Research (Award No. N00014-20-1-2184), Robert A. Welch Foundation (Grant No. A-1261), National Science Foundation (Grant No. PHY-2013771), King Abdulaziz City for Science and Technology (KACST).

X. N. and F. Y. thank A. Svidzinsky for his kind help during their visit at IQSE, Texas A&M University.

[1] T. B. Pittman, Y. H. Shih, D. V. Strekalov, and A. V. Sergienko, Optical imaging by means of two-photon quantum entanglement, Physical Review A **52**, R3429 (1995).
[2] R. S. Bennink, S. J. Bentley, and R. W. Boyd, "two-photon" coincidence imaging with a classical source, Physical review letters **89**, 113601 (2002).
[3] X.-H. Chen, Q. Liu, K.-H. Luo, and L.-A. Wu, Lensless ghost imaging with true thermal light, Optics letters **34**, 695 (2009).
[4] Y. Bromberg, O. Katz, and Y. Silberberg, Ghost imaging with a single detector, Physical Review A **79**, 053840 (2009).
[5] J. H. Shapiro, Computational ghost imaging, Physical Review A **78**, 061802 (2008).
[6] M. P. Edgar, G. M. Gibson, R. W. Bowman, B. Sun, N. Radwell, K. J. Mitchell, S. S. Welsh, and M. J. Padgett, Simultaneous real-time visible and infrared video with single-pixel detectors, Scientific reports **5**, 10669 (2015).
[7] N. Radwell, K. J. Mitchell, G. M. Gibson, M. P. Edgar, R. Bowman, and M. J. Padgett, Single-pixel infrared and visible microscope, Optica **1**, 285 (2014).
[8] G. A. Howland, D. J. Lum, M. R. Ware, and J. C. Howell, Photon counting compressive depth mapping, Optics express **21**, 23822 (2013).
[9] M.-J. Sun, M. P. Edgar, G. M. Gibson, B. Sun, N. Radwell, R. Lamb, and M. J. Padgett, Single-pixel three-dimensional imaging with time-based depth resolution, Nature communications **7**, 1 (2016).
[10] D. B. Phillips, M.-J. Sun, J. M. Taylor, M. P. Edgar, S. M. Barnett, G. M. Gibson, and M. J. Padgett, Adaptive foveated single-pixel imaging with dynamic supersampling, Science advances **3**, e1601782 (2017).
[11] M.-J. Sun, X.-Y. Zhao, and L.-J. Li, Imaging using hyperuniform sampling with a single-pixel camera, Optics letters **43**, 4049 (2018).
[12] M. Aβmann and M. Bayer, Compressive adaptive computational ghost imaging, Scientific reports **3**, 1 (2013).
[13] M.-J. Sun, M. P. Edgar, D. B. Phillips, G. M. Gibson, and M. J. Padgett, Improving the signal-to-noise ratio of single-pixel imaging using digital microscanning, Optics express **24**, 10476 (2016).
[14] T. Misaridis and J. A. Jensen, Use of modulated excitation signals in medical ultrasound. part iii: High frame rate imaging, IEEE transactions on ultrasonics, ferroelectrics, and frequency control **52**, 208 (2005).
[15] F. Ferri, D. Magatti, L. Lugiato, and A. Gatti, Differential ghost imaging, Physical review letters **104**, 253603 (2010).
[16] M. Sun, X. He, M. Li, *et al.*, Thermal light subwavelength diffraction using positive and negative correlations, Chinese Optics Letters **14**, 040301 (2016).
[17] F. Soldevila, P. Clemente, E. Tajahuerce, N. Uribe-Patarroyo, P. Andrés, and J. Lancis, Computational imaging with a balanced detector, Scientific Reports **6**, 1 (2016).
[18] Y. Zhao, Q. Chen, X. Sui, and H. Gao, Super resolution imaging based on a dynamic single pixel camera, IEEE Photonics Journal **9**, 1 (2017).
[19] M.-J. Sun, H.-Y. Wang, and J.-Y. Huang, Improving the performance of computational ghost imaging by using a quadrant detector and digital micro-scanning, Scientific reports **9**, 1 (2019).
[20] B. Luo, P. Yin, L. Yin, G. Wu, and H. Guo, Orthonormalization method in ghost imaging, Optics express **26**, 23093 (2018).
[21] Z. Zhang, X. Wang, G. Zheng, and J. Zhong, Hadamard single-pixel imaging versus fourier single-pixel imaging, Optics Express **25**, 19619 (2017).
[22] M.-J. Sun, L.-T. Meng, M. P. Edgar, M. J. Padgett, and N. Radwell, A russian dolls ordering of the hadamard basis for compressive single-pixel imaging, Scientific reports **7**, 1 (2017).
[23] V. Katkovnik and J. Astola, Compressive sensing computational ghost imaging, JOSA A **29**, 1556 (2012).
[24] Z. Sheng-Mei and Z. Peng, Correspondence normalized ghost imaging on compressive sensing, Chinese Physics B **23**, 054203 (2014).
[25] M. Lyu, W. Wang, H. Wang, H. Wang, G. Li, N. Chen, and G. Situ, Deep-learning-based ghost imaging, Scientific Reports **7**, 17865 (2017).
[26] Z.-H. Xu, W. Chen, J. Penuelas, M. Padgett, and M.-J. Sun, 1000 fps computational ghost imaging using led-based structured illumination, Optics express **26**, 2427 (2018).
[27] M. Le, G. Wang, H. Zheng, J. Liu, Y. Zhou, and Z. Xu, Underwater computational ghost imaging, Optics express **25**, 22859 (2017).
[28] L.-J. Li, W. Chen, X.-Y. Zhao, and M.-J. Sun, Fast optical phased array calibration technique for random phase modulation lidar, IEEE Photonics Journal **11**, 1 (2018).
[29] M. A. Herman, J. Tidman, D. Hewitt, T. Weston, and L. McMackin, A higher-speed compressive sensing camera through multi-diode design, in *Compressive Sensing II*, Vol. 8717 (International Society for Optics and Photonics, 2013) p. 871706.

[30] P. Dutta and P. Horn, Low-frequency fluctuations in solids: 1 f noise, Reviews of Modern physics **53**, 497 (1981).
[31] D. J. Field, Relations between the statistics of natural images and the response properties of cortical cells, Josa a **4**, 2379 (1987).
[32] P. Szendro, G. Vincze, and A. Szasz, Pink-noise behaviour of biosystems, European Biophysics Journal **30**, 227 (2001).
[33] J. Suo, L. Bian, Y. Xiao, Y. Wang, L. Zhang, and Q. Dai, A self-synchronized high speed computational ghost imaging system: A leap towards dynamic capturing, Optics & Laser Technology **74**, 65 (2015).
[34] W. Martienssen and E. Spiller, Coherence and fluctuations in light beams, American Journal of Physics **32**, 919 (1964).
[35] M. S. Keshner, 1/f noise, Proceedings of the IEEE **70**, 212 (1982)
.